

Dynamics of bubble growth and detachment in a viscous shear flow

G raldine Duhar and Catherine Colin

Citation: [Physics of Fluids \(1994-present\)](#) **18**, 077101 (2006); doi: 10.1063/1.2213638

View online: <http://dx.doi.org/10.1063/1.2213638>

View Table of Contents: <http://scitation.aip.org/content/aip/journal/pof2/18/7?ver=pdfcov>

Published by the [AIP Publishing](#)

Articles you may be interested in

[Compact bubble clusters in Newtonian and non-Newtonian liquids](#)

Phys. Fluids **26**, 053101 (2014); 10.1063/1.4874630

[Turbulent flow in rib-roughened channel under the effect of Coriolis and rotational buoyancy forces](#)

Phys. Fluids **26**, 045111 (2014); 10.1063/1.4871019

[On the dynamics and breakup of a bubble rising in a turbulent flow](#)

Phys. Fluids **23**, 103301 (2011); 10.1063/1.3648035

[Surface cleaning from laser-induced cavitation bubbles](#)

Appl. Phys. Lett. **89**, 074102 (2006); 10.1063/1.2337506

[A predictive model for the detachment of bubbles injected in a viscous shear flow with small inertial effects](#)

Phys. Fluids **16**, L31 (2004); 10.1063/1.1688231

The logo for AIP Applied Physics Letters. It features the letters 'AIP' in a large, white, sans-serif font on an orange background. To the right of 'AIP' is a vertical yellow bar, followed by the words 'Applied Physics Letters' in a smaller, white, sans-serif font.

is pleased to announce **Reuben Collins**
as its new Editor-in-Chief



Dynamics of bubble growth and detachment in a viscous shear flow

Géraldine Duhar and Catherine Colin^{a)}

Institut de Mécanique des Fluides de Toulouse, UMR CNRS/INPT/UPS 5502, 2 Avenue Camille Soula, 31400 Toulouse, France

(Received 24 August 2005; accepted 1 May 2006; published online 5 July 2006)

The quasistatic injection of air bubbles at the wall in a viscous shear flow is experimentally investigated by high-speed video pictures and image processing. The bubble radius and center of gravity position are determined throughout the growth. Experimental results are then used to validate a force balance model during bubble growth and after detachment for small bubble Reynolds numbers. The contact angles at the bubble foot calculated from the force balance agree well with those experimentally obtained from image processing. Finally, the force balance model is used to predict the departure bubble radius versus the gas flow rate and liquid flow shear rate.

© 2006 American Institute of Physics. [DOI: [10.1063/1.2213638](https://doi.org/10.1063/1.2213638)]

I. INTRODUCTION

Bubble growth and detachment from a wall is a mechanism encountered in many practical applications: bubble injection through pierced membranes or porous media in gas liquid contactors in chemical engineering, bubble vaporization on boilers or heat exchangers heated walls, cavitation. Predicting bubble sizes when they detach is crucial in these situations. For example, bubble size control is important to optimize interfacial area and mass transfer between two phases in chemical contactors. In nucleate boiling, micro-scale heat transfer is strongly dependent on nucleation and on bubble growth and detachment from the heated surfaces.

In most of the studies relating to bubble injection, gas is supplied from a chamber through an injection device (a small tube or a needle). Air bubbles are formed at the tube or needle outlet. The bubble growth rate depends both on the injection device and on the chamber volume. If the pressure drop through the injection device is high compared to the capillary pressure induced by the bubble formation, the volumetric gas flow rate Q is constant throughout the bubble growth.¹ If the chamber has a great volume and if the injection device has a low pressure drop, injection is characterized by a constant supply pressure:^{2,3} the bubble growth rate depends on the capillary pressure. This rate is weak at the beginning of the growth and increases as the capillary pressure decreases. Bubbling regimes depend on the injection device but also on the gas flow rate value. Three regimes for bubble formation have been identified,⁴ each of them depending on the gas flow rate. The quasistatic regime occurs at very low gas flow rates lower than $1 \text{ cm}^3/\text{s}$ and corresponds to a regular bubble injection. In the dynamic regime, for intermediate gas flow rates, injection becomes irregular with “pairing”—or “double bubbling” regime—with coalescence. In the third regime encountered for gas flow rates higher than $200 \text{ cm}^3/\text{s}$, bubble coalescence is very strong and a jet regime appears.⁵

Many studies have been performed in the past decades

on bubble growth and detachment from walls in stagnant or flowing liquid, with or without mass transfer (boiling, cavitation, injection). In several studies the prediction of bubble size at detachment is based on a force balance applied to the bubbles. In the quasistatic and dynamic regimes, bubble detachment is most of the time predicted from a force balance applied to a bubble assumed to be spherical.^{6–8} The difficulty of writing a force balance in this situation is due to the fact that some forces are unknown for a bubble attached to a wall. It is especially the case for drag and lift forces in the case of a bubble growing at the wall in a shear flow. The drag coefficient is often determined from experiments of bubble detachment in flowing liquid,⁹ or by the potential theory for inviscid liquids.¹⁰ Furthermore, determining the capillary force that acts on the triple solid-liquid-gas contact line and keeping the bubble attached to the wall requires the determination of the contact angle along the triple line.

Bubble formation in a liquid at rest has been modeled and numerically calculated by many authors.^{11–13} Oguz and Prosperetti¹¹ performed boundary-integral potential-flow calculations of bubble growth at the outlet of a needle and found bubble shape evolutions in very good agreement with experiments in a quiescent liquid or in an inviscid liquid flowing in parallel to the needle. The bubble shape is spherical at the beginning of the growth and becomes elongated with the formation of a neck before detachment. In others studies,^{12,13} the evolution of the bubble local curvature radius is calculated from the Rayleigh’s equation and the center of gravity vertical coordinate is deduced from a force balance. Bubble detachment naturally occurs as the thickness of the neck reaches zero. These models are able to calculate the evolution of nonspherical bubble shapes. They have been extended to bubble formation in a coflowing liquid¹⁴ and also in cross flow, but were limited to inviscid flows.¹⁵ The bubble radius at detachment predicted by these models is unfortunately very sensitive to the force balance used to calculate the position of the bubble center of gravity. Furthermore, such models cannot be applied to a bubble growing at the wall in a viscous cross flow.

The present paper is devoted to the study of bubble

^{a)}Electronic mail: colin@imft.fr

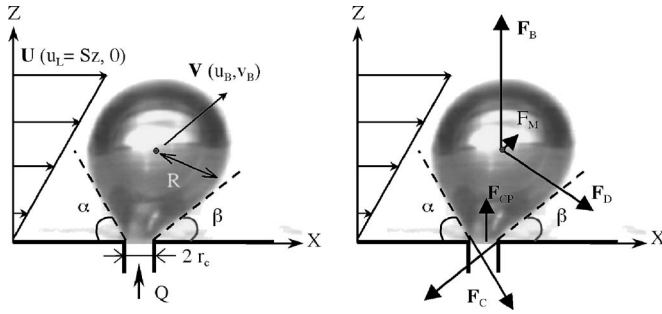


FIG. 1. Air bubble injected at the wall of a linear shear flow: geometry, velocities, and forces.

growth and detachment in a viscous shear flow. Bubbles are formed by air injection at the lower wall of a channel. The upper part of the channel is moved, creating a Couette flow. The bubble Reynolds numbers characteristic of the flow around the bubble are typically smaller than 1. Bubble growth and detachment are visualized by a high-speed video camera. The evolution of the bubble equivalent radius and of the center of gravity position are determined by image processing. Bubble motion just after detachment in the near wall region is also investigated. The drag and migration forces acting on the bubble are compared to theoretical expressions recently derived by Magnaudet *et al.*¹⁶ The expressions of these different forces are then extrapolated to the case of a bubble attached to the wall.

The forces acting on a bubble are detailed in Sec. II. The experimental setup and measurement techniques are described in Sec. III. Evolutions of the bubble radius and of the center of gravity position during the growth and after detachment are presented in Sec. IV. Bubble dynamics in the near wall region is investigated in Sec. V. Finally, a new force balance for a bubble growing at the wall in a viscous shear flow is derived for low bubble Reynolds numbers in Sec. VI and a criterion for bubble detachment is proposed in Sec. VII.

II. FORCES ACTING ON A BUBBLE IN A VISCOUS SHEAR FLOW

For a bubble growing on a wall (Fig. 1), the force balance can be written⁸ as

$$\frac{4}{3}\pi R^3 \rho_G \mathbf{g} + \mathbf{F}_c - \int_{S_B} (p_L - \rho_L g Z) \mathbf{n} dS - \int_{S_f} p_G \mathbf{n} dS + \int_{S_B} \boldsymbol{\tau}_L \cdot \mathbf{n} dS = \mathbf{0}, \quad (1)$$

where the first term is the bubble weight, \mathbf{F}_c is the capillary force, p_L is the pressure in the liquid, $\boldsymbol{\tau}_L$ is the deviatoric stress tensor due to viscous effects, p_G is the pressure inside the bubble, S_B the bubble surface exposed to liquid flow, and S_f the surface of the bubble foot in contact with the cavity of radius r_c . R is the bubble equivalent radius based on the gas volume limited by S_B and S_f . The third and fourth terms of Eq. (1) can also be expressed versus the reference pressure p_c in the liquid at the wall $Z=0$:

$$\begin{aligned} & - \int_{S_B} (p_L - \rho_L g Z) \mathbf{n} dS - \int_{S_f} p_G \mathbf{n} dS \\ & = - \int_{S_B + S_f} (p_c - \rho_L g Z) \mathbf{n} dS \\ & + \int_{S_f} (p_c - \rho_L g Z - p_G) \mathbf{n} dS - \int_{S_B} (p_L - p_c) \mathbf{n} dS \\ & = \int_{S_B + S_f} \rho_L g Z \mathbf{n} dS + \int_{S_f} (p_c - p_G) \mathbf{n} dS \\ & - \int_{S_B} (p_L - p_c) \mathbf{n} dS. \end{aligned} \quad (2)$$

The first term of the rhs of Eq. (2) is the Archimedes force that can be grouped with the bubble weight into the buoyancy force:

$$\mathbf{F}_B = (\rho_G - \rho_L) \frac{4}{3} \pi R^3 \mathbf{g}. \quad (3)$$

The second term was identified as the “contact pressure” force by Cohran and Aydelott¹⁷ (see also Klausner *et al.*¹⁸). This force is a function of the surface tension σ_L and the orifice radius r_c :

$$\begin{aligned} \mathbf{F}_{CP} &= \int_{S_f} (p_c - p_G) \mathbf{n} dS \\ &= (p_c - p_G) \pi r_c^2 \mathbf{e}_z = (p_i - \rho_L g H - p_G) \pi r_c^2 \mathbf{e}_z \\ &= \left(\frac{2\sigma_L}{R} - \rho_L g H \right) \pi r_c^2 \mathbf{e}_z \\ &\approx \frac{2\sigma_L \pi r_c^2}{R} \mathbf{e}_z \quad \text{if } \rho_L g H \ll \frac{2\sigma_L}{R}, \end{aligned} \quad (4)$$

where p_i is the liquid pressure at the bubble top and H is the bubble height.

Equation (1) then becomes

$$\underbrace{\mathbf{F}_c + \mathbf{F}_{CP} + \mathbf{F}_B}_{\text{static forces}} - \underbrace{\int_{S_B} (p_L - p_c) \mathbf{n} dS + \int_{S_B} \boldsymbol{\tau}_L \mathbf{n} dS}_{\text{hydrodynamic forces}} = \mathbf{0}. \quad (5)$$

The two last terms of Eq. (5) are the hydrodynamics forces acting on the bubble such as the drag, the migration, and the unsteady forces. Among the static forces, the capillary force is expressed as

$$\begin{aligned} \mathbf{F}_c &= \int_0^{2\pi} r_c \sigma_L \mathbf{t}(\theta) d\theta \\ &= - \int_0^{2\pi} r_c \sigma_L \cos \phi(\theta) \cos \theta d\theta \mathbf{e}_x \\ &\quad - \int_0^{2\pi} r_c \sigma_L \sin \phi(\theta) d\theta \mathbf{e}_z, \end{aligned} \quad (6)$$

where \mathbf{t} is the vector tangent to the interface and perpendicular to the contact line, \mathbf{e}_x and \mathbf{e}_z are the unit vectors parallel and perpendicular to the wall, ϕ is the contact angle along

the contact line, which is a function of the polar angle θ . Assuming that $\phi(\theta)$ evolves linearly with θ and knowing that $\phi(0)=\beta$ and $\phi(\pi)=\alpha$ Klausner *et al.*¹⁷ obtained the following expression for the capillary force:

$$\mathbf{F}_C = 1.25 \times 2r_c \sigma_L \frac{\pi(\alpha - \beta)}{\pi^2 - (\alpha - \beta)^2} (\sin \alpha + \sin \beta) \mathbf{e}_x - 2r_c \sigma_L \frac{\pi}{(\alpha - \beta)} [\cos \beta - \cos \alpha] \mathbf{e}_z, \quad (7)$$

α and β are the advancing and receding contact angles, respectively (Fig. 1).

$$\mathbf{F}_D = 4\pi\mu_L R \left\{ \left[(u_L - u_B) \left(1 + \frac{3}{8}\kappa + \frac{9}{64}\kappa^2 + \frac{27}{512}\kappa^3 \right) + \frac{1}{8}RS\kappa^2 \left(1 + \frac{3}{8}\kappa \right) + O(\kappa^4) \right] \mathbf{e}_x - v_B \left[1 - \frac{3}{4}\kappa - \frac{9}{64}\kappa^4 + O(\kappa^5) \right]^{-1} \mathbf{e}_z, \right\} \quad (8)$$

where $\mathbf{U} = u_L \mathbf{e}_x = S z \mathbf{e}_x$ is the liquid velocity, S the shear rate (constant), $\mathbf{V} = u_B \mathbf{e}_x + v_B \mathbf{e}_z$ the bubble velocity. This expression is valid for $\text{Re}_B \ll 1$ and for $\kappa = R/z < 1$, where z is the distance of the bubble center to the wall.

The migration force includes three contributions¹⁶: \mathbf{F}_M^δ [see Eqs. (53) and (38) of Magnaudet *et al.*¹⁶] is due to bubble deformation, \mathbf{F}_{Sl} [see Eq. (44a) of Ref. 16] is the slip-induced lift force and \mathbf{F}_{Sh} [see Eqs. (56a) and (47a)] the shear-induced lift force:

$$\mathbf{F}_M = \mathbf{F}_M^\delta + \mathbf{F}_{Sl} + \mathbf{F}_{Sh}, \quad (9)$$

$$\mathbf{F}_M^\delta = \left[\frac{4}{5} \frac{\pi\mu_L^2}{\sigma_L} R^2 S v_B \left(1 + \frac{3}{8}\kappa \right) + O(\kappa^2) \right] \mathbf{e}_x + \frac{\pi\mu_L^2 R}{\sigma_L} \left[\frac{4}{5} RS(u_L - u_B) \left(1 + \frac{9}{8}\kappa + \frac{63}{64}\kappa^2 \right) + \frac{3}{10}(u_L - u_B)^2 \kappa^2 + \frac{169}{70} R^2 S^2 \kappa^2 + O(\kappa^3) \right] \mathbf{e}_z, \quad (10)$$

$$\mathbf{F}_{Sl} = \left(\frac{\pi}{4} \rho_L R^2 (u_L - u_B)^2 (1 + 0.125\kappa - 0.516\kappa^2) + O(\kappa^3) \right) \mathbf{e}_z, \quad (11)$$

$$\mathbf{F}_{Sh} = - \left[\frac{5}{8} \pi \rho_L R^3 S v_B \left(\kappa^{-1} - \frac{121}{120} \right) + O(\kappa) \right] \mathbf{e}_x - \frac{\pi}{4} \rho_L R^2 \times \left[- \frac{11}{6} RS(u_L - u_B) \left(\kappa^{-1} + \frac{99}{88} + 1.023\kappa \right) + \frac{11}{18} R^2 S^2 (1 + 0.375\kappa) + O(\kappa^2) \right] \mathbf{e}_z. \quad (12)$$

Expressions of the hydrodynamic forces are generally unknown for a bubble growing on a wall. Some expressions have, however, been derived for a bubble in the wall vicinity in the case of large or small bubble Reynolds numbers $\text{Re}_B = 2R|\mathbf{U} - \mathbf{V}|/\nu_L$, where \mathbf{U} is the liquid velocity and \mathbf{V} the bubble velocity. At low bubble Reynolds numbers, $\text{Re}_B \ll 1$, the recent results of Magnaudet *et al.*¹⁶ give the expressions of drag \mathbf{F}_D , migration \mathbf{F}_M , and unsteady \mathbf{F}_U forces for a bubble moving close to a wall. The drag force includes the quasistatic Stokes drag and a Faxen correction due to wall vicinity [the second term on the X component in Eq. (8)]. The expression of the drag force is given in Eqs. (23a) and (51a) of Ref. 16:

Equations (10)–(12) are valid for $\gamma \text{Ga} \ll \kappa^2 \ll 1$ and $\text{Ga} \ll \kappa \ll 1$, with $\gamma = \mu_L S / \rho_L R g$ the dimensionless shear gradient and $\text{Ga} = \rho_L^2 R^3 g / \mu_L^2$ the Galileo number.

The unsteady force \mathbf{F}_U includes added mass and history effects.¹⁹ It is expected to play a role only at the beginning of the growth and when the detachment occurs. Since the bubble growth is quasistatic in our study (see Sec. IV), the added mass force estimated by Thorncroft *et al.*⁸ for a growing bubble near a wall is very low (10^{-8} N) in comparison of other forces (10^{-6} N). At detachment, bubble acceleration is strong and the added mass and the history forces should be taken into account. Unfortunately, the expression of the history force provided by Magnaudet¹⁸ is not valid for large bubble accelerations. This force will therefore be disregarded in the following.

In conclusion, during the growth, the buoyancy, the drag, the contact pressure, the capillary, and the migration forces play a role. In the vertical direction, the buoyancy, the contact pressure, and the migration forces promote the bubble detachment, whereas the drag and the capillary forces keep the bubble attached to the wall. In the horizontal direction, the drag and the migration forces act for bubble detachment against the capillary force.

After bubble detachment, only the buoyancy, the drag, and the migration forces will be considered. Bubble dynamics in the near wall region will be investigated in Sec. V.

III. EXPERIMENTAL SETUP AND MEASUREMENT TECHNIQUES

A. Description of the experimental setup

The experimental setup (Fig. 2) consists of a horizontal channel in the shape of a torus with a rectangular cross section, filled with a viscous liquid. An injection device (a cap-

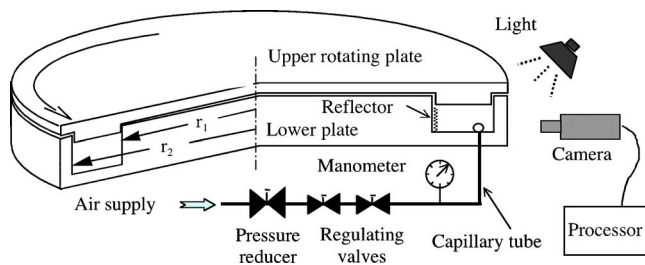
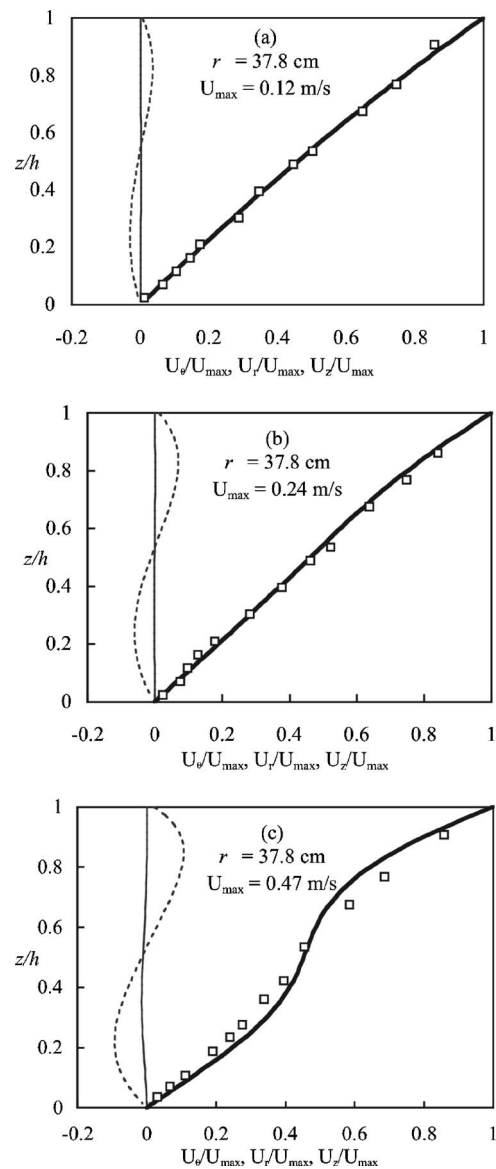


FIG. 2. Experimental setup of injection in a Couette flow.

illary tube of 0.3 mm inner diameter) allows bubble formation at the channel lower wall for constant gas flow rates Q between 2 to 40 mm³/s. The channel of 2.15 cm of height and 9 cm of width (the cross section between the radii $r_1=32$ cm and $r_2=41$ cm) is built in a cylindrical Plexiglas plate. The channel upper wall belongs to the upper plate, which can be rotated, creating a Couette flow inside the channel. Silicon oil (47V50, properties at 20 °C: density $\rho_L=960$ kg/m³, dynamic viscosity $\mu_L=0.051$ 22 Pa s, surface tension $\sigma_L=0.0207$ N/m) is chosen to obtain a laminar flow for shear rates S up to 20 s⁻¹. Due to the circular geometry, the centrifugal force induces a secondary flow. Therefore, the flow was carefully checked by Laser Doppler Velocimetry measurements and by numerical simulations performed with the code Jadim developed at IMFT. A bubble injector is positioned at the radial position $r=37.8$ cm in the channel lower wall. At this position the liquid flow is unidirectional for shear rates up to 15 s⁻¹. The computed components of the liquid velocity at $r=37.8$ cm are plotted in Fig. 3 and compared to LDV measurements, for three shear rates. These velocity profiles are scaled by U_{\max} , the velocity of the plate at $r=37.8$ cm. For $U_{\max}=0.12$ m/s and $U_{\max}=0.24$ m/s, the profiles of the azimuthal velocity are almost linear. For $U_{\max}=0.47$ m/s, the secondary flow becomes significant and the azimuthal velocity profile is no longer linear. The values of the local shear rate in the wall vicinity are, respectively, 6.2, 11.8, and 18 s⁻¹ for $U_{\max}=0.12$, 0.24, and 0.47 m/s and the corresponding values of the global shear rate over the channel height are $U_{\max}/h=5.6$, 11.2, and 21.9 s⁻¹. Except for the higher shear rate, the liquid flow will be considered as unidirectional and bubble trajectories in the field of view of the camera will remain in a plane.

The bubble injector is a capillary tube of 0.3 mm inner diameter, which crosses the channel lower wall. Air is supplied by a compressor at 7 bar, its pressure is regulated by a pressure reducer. The air mass flow rate is adjusted by two regulating valves. The pressure loss through the capillary tube and the control valves ranges between 100 and 150 m bar. It is higher than the capillary pressure generated by the bubble formation. Air is thus injected with a constant volume flow rate Q throughout the bubble growth. The time-evolution of the bubble radius R has the following form:

$$R(t) = \left(\frac{3Qt}{4\pi} \right)^{1/3}. \quad (13)$$

FIG. 3. Velocity profiles for (a) $S=6.2$ s⁻¹, (b) $S=11.8$ s⁻¹, and (c) $S=18$ s⁻¹. Computed values: —, U_θ/U_{\max} ; - - -, U_r/U_{\max} ; — · —, U_z/U_{\max} ; measured values: □, U_θ/U_{\max} .

B. Visualization and image processing

Measurements are obtained from high-speed video recordings and image processing. Bubble growth and detachment are filmed by a rapid video camera Kodak Ektapro EM at frequencies between 250 and 2000 images per second. The camera CCD sensor has a matrix of 192 pixels \times 239 pixels. Bubble departure diameters range between 1 and 3 mm. The camera is equipped with a lens of focal distance 105 mm. The size of the pictures (4 mm \times 5 mm) allows a precise detection of the bubble outline during the growth. The camera films the bubbles through a Plexiglas wall. Two projectors of 1200 W, on both sides of the camera, light the reflector diffuser located on the channel inner wall (see Fig. 2). Direct lighting on the bubble is eliminated by masks in order to avoid direct reflections on the bubble interface, which could lead to significant errors in the bubble size measurement. Pictures are directly recorded on a numerical processor

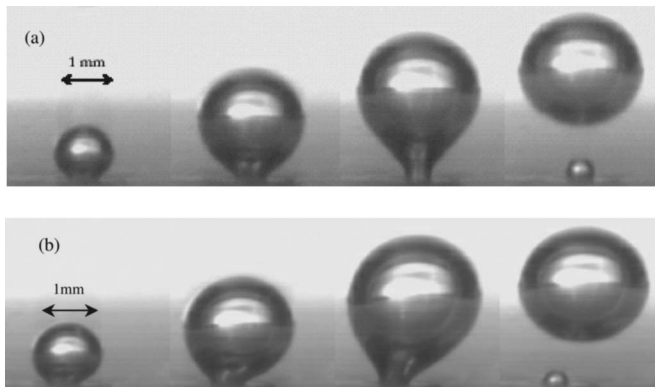


FIG. 4. Growth of air bubbles injected in silicon oil (47V50): (a) for $Q \approx 2.5 \text{ mm}^3/\text{s}$ and $S \approx 0 \text{ s}^{-1}$; (b) for $Q \approx 2.5 \text{ mm}^3/\text{s}$ and $S \approx 5.5 \text{ s}^{-1}$.

Kodak Ektapro that can store 1600 images per run. They are then transferred to the hard disk of a microcomputer using an analog-digital converter Mirovideo DC30+. Some pictures of bubble growth are presented in Fig. 4 for $Q = 2.34 \text{ mm}^3/\text{s}$ in a quiescent liquid and for $Q = 2.76 \text{ mm}^3/\text{s}$ in a shear flow with $S = 5.5 \text{ s}^{-1}$.

Images are then processed by using the software Optimas to determine the bubble geometrical characteristics during the growth. Image processing consists of (Fig. 5):

- (i) a division by a background image (without bubble) that allows an increase in the contrast,
- (ii) the application of a median filter in order to smooth the bubble outline [Fig. 5(b)],
- (iii) the determination of the gray levels histogram,
- (iv) the choice of a threshold on the gray levels, and a binarization [Fig. 5(c)],
- (v) the detection of the bubble outline and a sampling of this outline on 256 points.

From the bubble outline coordinates, the time evolutions of bubble geometrical characteristics (equivalent radius R , center of gravity coordinates x and z in horizontal and vertical directions) are calculated by using the software Matlab. The bubble real size and position are obtained after image calibration. A calibrated grid placed inside the channel just above the injector is filmed by the camera. Calibration factors are determined in the longitudinal direction (110 pixels/mm) and in the vertical direction (120 pixels/mm) to correct parallax errors due to the channel curvature and the contrast of optical indexes between oil and Plexiglas.

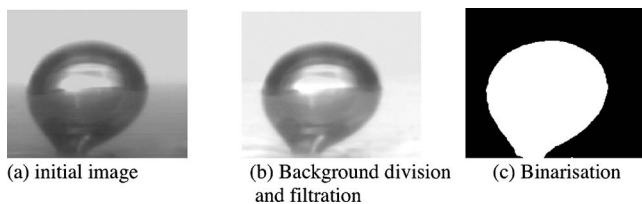


FIG. 5. Different steps of image processing.

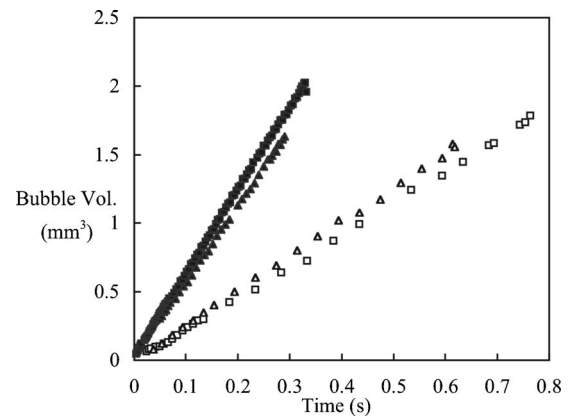


FIG. 6. Volume of bubble injected in silicon oil for: \square $Q = 2.34 \text{ mm}^3/\text{s}$ and $S = 0$; \triangle , $Q = 2.60 \text{ mm}^3/\text{s}$ and $S = 9.9 \text{ s}^{-1}$; \blacksquare , $Q = 5.53 \text{ mm}^3/\text{s}$ and $S = 0$; \blacktriangle , $Q = 5.16 \text{ mm}^3/\text{s}$ and $S \approx 10.8 \text{ s}^{-1}$.

C. Measurement accuracy

The different steps of visualization and image processing induce measurement uncertainties. First of all the spatial resolution of the camera is limited: the field of view is $5 \text{ mm} \times 4 \text{ mm}$, corresponding to 239×192 pixels. An error of one pixel generates an error of 0.02 mm . The error due to the filtering operation is negligible, about 0.1% , on the bubble diameter. On the other hand, calibration generates an error of about 3% on the measurements. Finally, a variation

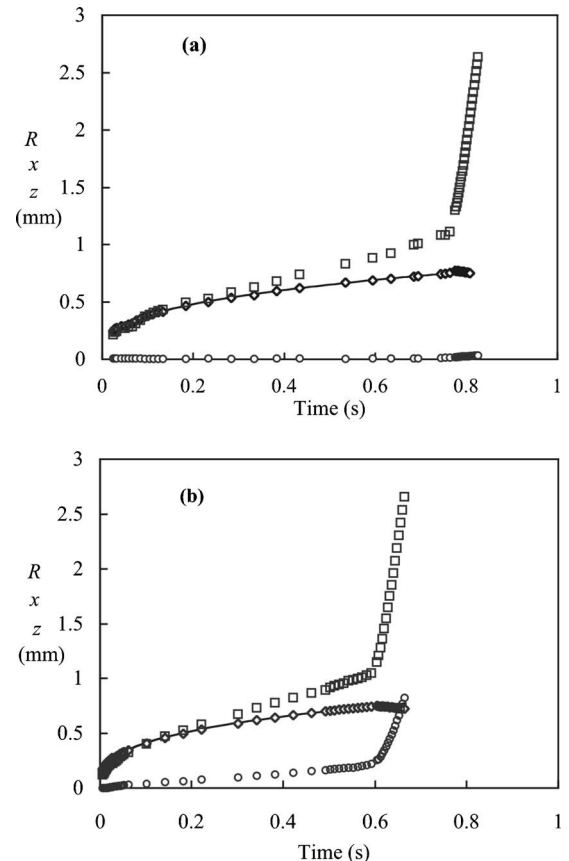


FIG. 7. Time evolutions of bubble radius and position of the center of gravity for (a) $Q = 2.34 \text{ mm}^3/\text{s}$, $S = 0 \text{ s}^{-1}$; and (b) $Q = 2.60 \text{ mm}^3/\text{s}$, $S = 9.9 \text{ s}^{-1}$: \diamond , R ; —, Eq. (13), \circ , x , \square , z .

TABLE I. Test parameters: gas flow rate, liquid flow shear rate, bubble radius at detachment, frequency of formation.

Q (mm ³ /s)	S (s ⁻¹)	R_{det} (mm)	f (Hz)
2.34	0	0.753	1.29
2.76	5.6	0.743	1.63
2.60	9.9	0.719	1.77
5.53	0	0.776	2.90
5.55	5.2	0.768	2.97
5.16	10.8	0.715	3.17
9.87	0	0.789	4.78
10.34	5	0.785	5.10
11.27	10.52	0.751	6.35
24.95	0	0.815	10.98
25.26	5	0.791	12.17
27.94	10.52	0.778	14.25
40.36	0	0.863	14.92
40.15	5	0.833	16.55
40.69	10.52	0.815	17.92

of ten gray levels on the binarization threshold leads to a difference of 0.01 mm on the bubble radius and on the centre of gravity coordinates. Thus, after all the operations, the measurement uncertainty on the bubble diameter is estimated to ± 0.035 mm.

IV. EXPERIMENTAL RESULTS

In Table I, the values of the test parameters are gathered: the airflow rate Q , the shear rate S , the bubble radius at detachment R_{det} and the bubble formation frequency f for each run. Experiments have been performed for gas flow rates Q up to 40 mm³/s and for shear rates S up to 11 s⁻¹. Image processing is limited to the lowest gas flow rates ($Q < 6$ mm³/s) for the investigation of the bubble growth. At higher gas flow rates bubble interactions are strong and the growing bubble is in contact with the preceding departing bubble. It is therefore difficult to extract the growing bubble outline. For high gas flow rate, bubble characteristics are only determined after detachment.

In a first time, we can notice that the radius at detachment R_{det} increases with the gas flow rate Q and decreases with the shear rate S . The formation frequency increases with the gas flow rate and with the shear rate.

In our experiments the range of gas flow rates Q (2 to 40 mm³/s) corresponds to quasistatic regimes of bubble injection: $Q < Q_{\text{crit}}$. A value of Q_{crit} is given by Oguz and Prosperetti¹¹ for low viscous flows:

$$Q_{\text{crit}} \approx \pi \left(\frac{16}{3g^2} \right)^{1/6} \left(\frac{\sigma_L r_c}{\rho_L} \right)^{5/6} \approx 163 \text{ mm}^3/\text{s}. \quad (14)$$

We also verified that our injection device provides a constant volumetric flow rate. Figure 6 shows that bubble volume

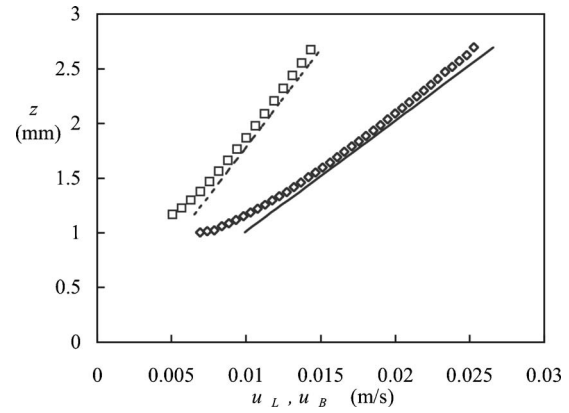


FIG. 8. Bubble and liquid velocities for: $Q=2.76$ mm³/s and $S=5.6$ s⁻¹: \square , u_B , - - -, u_L ; $Q=2.60$ mm³/s and $S=9.9$ s⁻¹: \diamond , u_B , —, u_L .

varies linearly with time whatever the gas flow rate and the shear rate.

From image processing, time evolutions of bubble equivalent radius R and of center of gravity coordinates x and z are determined. In Figs. 7(a) and 7(b), these evolutions are plotted for $Q=2.34$ mm³/s and $S=0$ and for $Q=2.60$ mm³/s and $S=9.9$ s⁻¹. The bubble radius follows the $t^{1/3}$ law given by Eq. (13). It is characterized by a strong variation at the beginning of the growth and a weaker increase before detachment. After detachment, the radius is constant equal to R_{det} value. During the beginning of the growth the coordinate z follows the radius R , the bubble is spherical. Later z becomes greater than R : a neck appears between the injector and the spherical part of the bubble (Fig. 4). The value of the coordinate x is characteristic of the bubble orientation in the downstream direction of the flow under the velocity gradient. After detachment, the bubble moves up vertically in a quiescent liquid while it follows the shear rate in a flowing liquid. These results are presented for one bubble but the reproducibility of the experiments was carefully checked²⁰ and the behavior is identical for all the bubbles injected with the same air flow rate in the same liquid flow.

Bubble velocities after detachment in the X direction are plotted in Fig. 8 for Q around 2.7 mm³/s and different shear rates. The bubble velocity u_B reaches very quickly the liquid velocity u_L . In the Z direction perpendicular to the wall, the bubble velocity v_B is about 5 to 6 mm/s after the detachment. In our study, the bubble Reynolds numbers based on the bubble relative velocity $|\mathbf{U} - \mathbf{V}|$ are typically smaller than 1. The hydrodynamic regime experienced by the bubble during its growth and after its detachment is therefore weakly inertial. The time evolutions of the coordinates x and z are fitted by polynomial laws. The bubble velocities u_B and v_B in the horizontal and vertical directions are calculated from the derivation of these polynomial laws. The evolutions of the bubble radius, of the center of gravity positions and velocities are then used to calculate the different forces acting on the bubble during its growth and after its detachment.

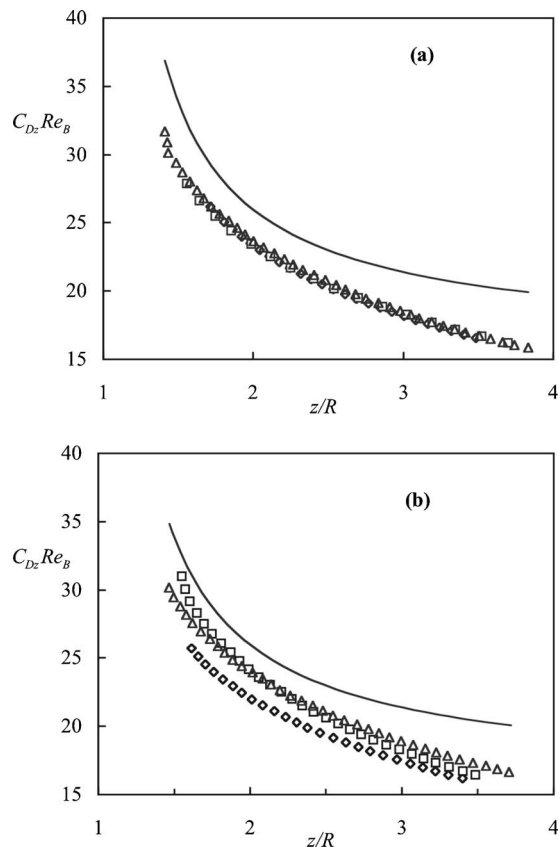


FIG. 9. Drag coefficient in the normal direction to the wall for $Q \approx 2.5 \text{ mm}^3/\text{s}$ (a) and for $Q \approx 5.4 \text{ mm}^3/\text{s}$ (b) \diamond , $S=0 \text{ s}^{-1}$, \square , $S \approx 5.5 \text{ s}^{-1}$, Δ , $S \approx 10 \text{ s}^{-1}$, —, Eq. (16).

V. BUBBLE MOTION IN THE NEAR WALL REGION

When a bubble is in motion near a wall, the force balance can be written as

$$(\rho_G - \rho_L) \frac{4}{3} \pi R^3 \mathbf{g} + \mathbf{F}_D + \mathbf{F}_M = \mathbf{0}. \quad (15)$$

The different forces in Eq. (15) are, respectively, the buoyancy force, viscous drag force \mathbf{F}_D given by Eq. (8), migration force \mathbf{F}_M given by Eq. (9). Unsteady forces are neglected.

By using the expression of the Z component of \mathbf{F}_M it is possible to estimate the drag coefficient for a bubble departing from a wall. The drag coefficient experimentally measured from the force balance (15) is compared in Fig. 9 to the theoretical expression given by Magnaudet *et al.*:¹⁶

$$C_{D_z} \approx \frac{16}{\text{Re}_B} \left[1 - \frac{3R}{4z} - \frac{9}{64} \left(\frac{R}{z} \right)^4 \right]^{-1}. \quad (16)$$

A quasisystematic shift is noted between the evolutions of the theoretical and the experimental drag coefficients. Equation (16) is valid close to the wall ($z/R \approx 1.1$) and the discrepancy between the theoretical and measured values cannot be explained by the limit of validity of this equation. It seems that for the gas flow rates under investigation a strong interaction between the bubbles does exist. The bubble just detached from the wall is pushed by the following bubble growing on the wall. The bubble velocity in the vertical direction is therefore larger than the velocity of an isolated bubble and the drag coefficient is lower. The shift seems to

increase when the gas flow rate increases because the distance between the bubbles decreases. In the force balance (15), we can note that the Z component of the migration force F_{M_z} is about equal to 10^{-9} N , which is much smaller than drag and buoyancy forces around 10^{-5} N .

In the X direction parallel to the wall, the force balance can be written as

$$F_{D_x} + F_{M_x} = 0, \quad (17)$$

where F_{D_x} , F_{M_x} are, respectively, the X component of the drag and the migration forces given by Eqs. (8)–(12). The evolution of these two forces after bubble detachment can be seen in the right part of Fig. 13, later. The force balance is also plotted in this figure. We observe an unbalance of the forces as the bubble is detaching. This is due to the fact that the unsteady forces are not taken into account. After the detachment for $t > 0.64 \text{ s}$ the drag force balances the migration force.

The analysis of the bubble motion near the wall will then be used to extrapolate the different forces for a bubble growing on a wall. During the growth, the bubble acceleration is very small it is therefore reasonable to neglect the unsteady forces. In the Z direction, the drag coefficient can be extrapolated from the experimental data of Fig. 9 to a value of $38/\text{Re}_B$ at the wall ($R/z=1$). In the X direction, after detachment when the bubble acceleration becomes small, the drag force balances the migration force in the wall vicinity. A rigorous extrapolation of these two forces for a bubble growing on the wall would require an expansion at higher order than κ^3 in Eq. (8)–(12). We can remark that the migration force estimated for $\kappa=1$ is two orders of magnitude smaller than the drag force in the X direction ($F_{M_x} \approx 10^{-9} \text{ N}$ and $F_{D_x} \approx 10^{-7} \text{ N}$) and three orders of magnitude smaller than the buoyancy force in the Z direction ($F_{M_z} \approx 10^{-8} \text{ N}$ and $F_{B_z} \approx 10^{-5} \text{ N}$). Thus, the extrapolation of the migration force to the wall will not affect the accuracy of the force balance. More questionable is the extrapolation of the X component of the drag force for $\kappa=1$. However, this extrapolation can be justified. In Eq. (8) the Faxen correction is only 10% of the total force. In the Stokes drag the term of order κ^3 ($27/512 \approx 0.053$) is 4% of the total expansion of order κ^2 for $\kappa=1$ ($1+3/8+9/64=1.516$). The contribution of higher order terms in κ^4 , κ^5 , ..., is expected to be still weaker. It is therefore reasonable to use an extrapolation of Eq. (8) for $\kappa=1$ to calculate F_{D_x} for a bubble growing on a wall.

VI. DYNAMICS OF BUBBLE GROWTH AND DETACHMENT

The forces involved in the dynamics of bubble growth are the buoyancy, the drag, the migration, the capillary, and the contact pressure forces. Since the bubble growth is quasistatic, the unsteady forces are neglected.

A. In a quiescent liquid

In this case, the force balance is written only in the Z direction:

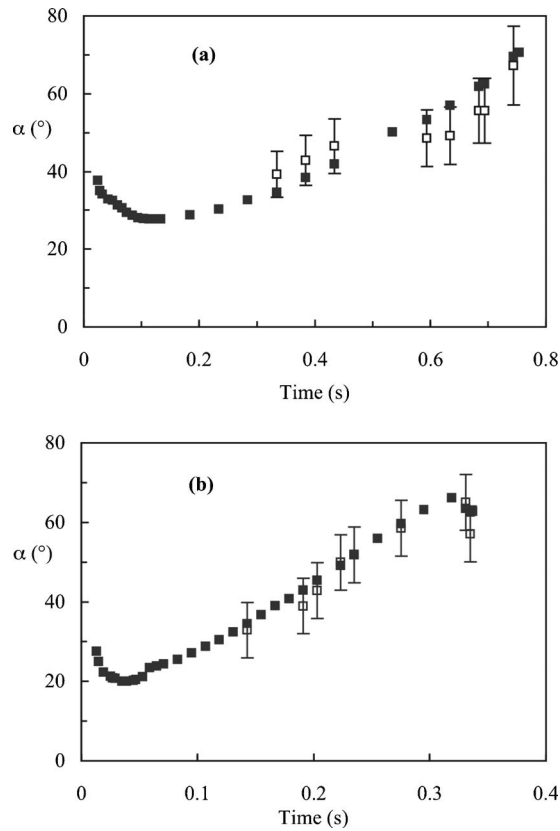


FIG. 10. Contact angles of a growing bubble in a quiescent flow for $Q=2.34 \text{ mm}^3/\text{s}$ (a) and $Q=5.6 \text{ mm}^3/\text{s}$ (b): ■, calculated from Eq. (19); □, measured from image processing.

$$F_{Bz} + F_{Cz} + F_{CPz} + F_{Dz} + F_{Mz} = 0, \quad (18)$$

where F_{Mz} is equal to zero and the capillary force reduces to $-2\pi\sigma_L r_c \sin \alpha$, where α is the value of the contact angle ($\alpha = \beta$). Equation (18) becomes then

$$(\rho_L - \rho_G) \frac{4}{3} \pi R^3 g - 2\pi\sigma_L r_c \sin \alpha + \frac{2\pi\sigma_L}{R} r_c^2 - 4\pi\mu_L R v_B k_z = 0, \quad (19)$$

k_z is the coefficient taking into account the presence of the wall in the Stokes drag: $k_z = 1$ far from the wall and k_z is approximately equal to 38/16 for a bubble growing on the wall in our experiments (Fig. 9). In Eq. (19), the value of the contact angle α is unknown. This equation can be solved by using the experimental values of R and v_B throughout the bubble growth. In Fig. 10, the values of α calculated from Eq. (19) are compared to the experimental values determined from image processing. The calculated values are in good agreement with the experiments, which validates the force balance (19) for a bubble growing in a quiescent viscous liquid. We can remark that at the beginning of the growth α decreases and the bubble reaches a spherical shape. Then α increases due to the neck formation. The detachment occurs for a value of α close to 70° and not for its maximum value 90° .

In Fig. 11, the different forces involved in Eq. (19) are plotted. At the beginning of the growth, the capillary and the contact pressure forces are dominant. They balance each

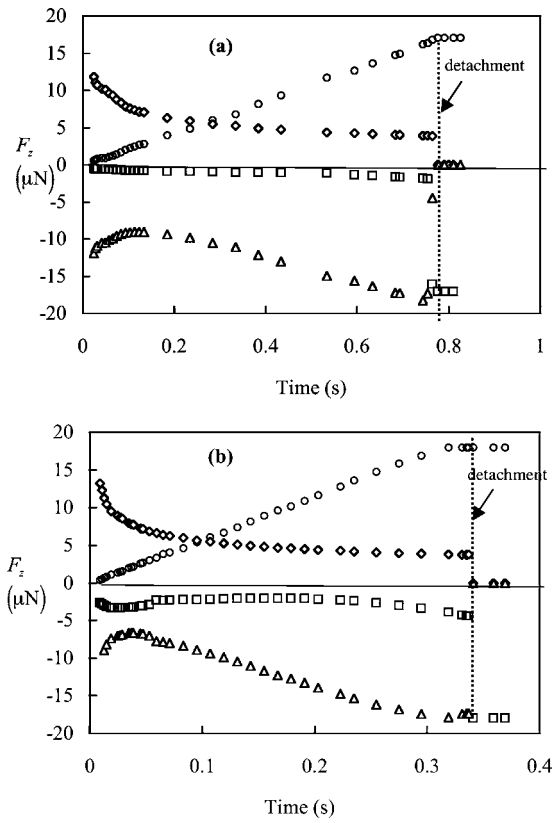


FIG. 11. Forces acting on a growing bubble for $Q=2.34 \text{ mm}^3/\text{s}$ (a) and $Q=5.6 \text{ mm}^3/\text{s}$ (b) ○, F_{Bz} , △, F_{Cz} , ◇, F_{CPz} , □, F_{Dz} .

other. As the bubble radius increases, the buoyancy force becomes significant. The contact pressure force decreases whereas the capillary force continues to grow due to higher values of the contact angle. The effect of the drag force is small but not negligible, especially for $Q=5.53 \text{ mm}^3/\text{s}$, where it becomes of the same order of magnitude as the contact pressure force. The four forces play a role in the dynamics of the bubble growth and they must be taken into account in a model for the prediction of the bubble diameter at detachment. After bubble detachment, the drag force balances the buoyancy force.

B. In a shear flow

The force balance can be written in the X and Z directions:

$$\begin{aligned} F_{Cx} + F_{Dx} + F_{Mx} &= 0, \\ F_{Bz} + F_{Cz} + F_{CPz} + F_{Dz} + F_{Mz} &= 0. \end{aligned} \quad (20)$$

The two components of the capillary force are given by Eq. (7).

In the X direction, after extrapolation of the expressions of the drag and migration forces for $\kappa=1$, the balance becomes

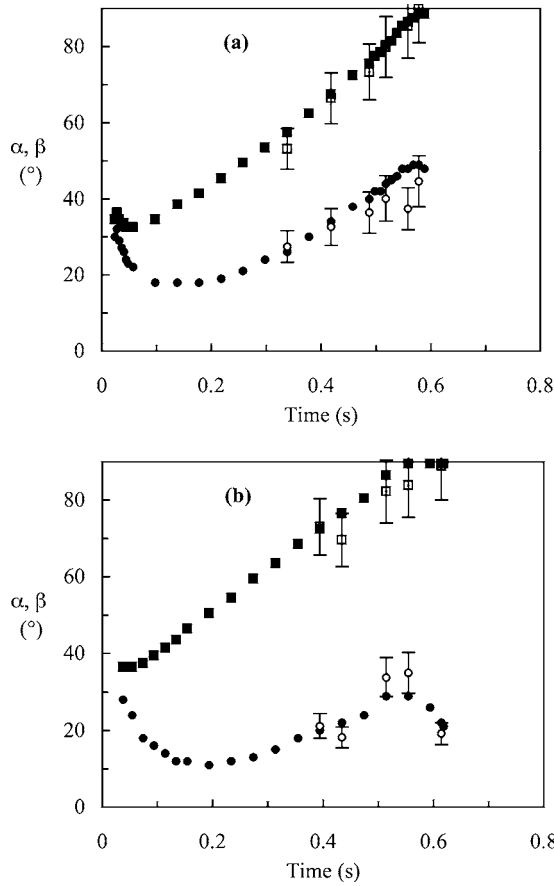


FIG. 12. Contact angles of a growing bubble for $Q=2.6 \text{ mm}^3/\text{s}$ and two shear rates $S=5.6 \text{ s}^{-1}$ (a) and $S=9.9 \text{ s}^{-1}$: \blacksquare , α and \bullet , β calculated from Eqs. (21) and (22); \square , α and \circ , β measured from image processing.

$$\begin{aligned}
 & -1.25 \times 2\sigma_L r_c \frac{\pi(\alpha - \beta)}{\pi^2 - (\alpha - \beta)^2} (\sin \alpha + \sin \beta) \\
 & + \frac{11}{8} \mu_L \pi R \left[4(u_L - u_B) - \frac{1}{2} RS \right] \\
 & + \left(\frac{11}{10} \frac{\mu_L^2}{\sigma_L} - \frac{1}{192} \rho_L R \right) \pi R^2 S v_B = 0.
 \end{aligned} \quad (21)$$

In the Z direction we obtain

$$\begin{aligned}
 & (\rho_L - \rho_G) \frac{4}{3} \pi R^3 g - 2\sigma_L r_c \frac{\pi}{\alpha - \beta} (-\cos \alpha + \cos \beta) \\
 & + \frac{2\pi\sigma_L}{R} r_c^2 - 4\pi\mu_L R v_B k_z + \frac{\pi\mu_L R^2}{\sigma_L} [0.3(u_L - u_B)^2 \\
 & + 2.488(u_L - u_B)RS + 2.414R^2S^2] \\
 & + \frac{\pi\rho_L R^2}{4} [0.609(u_L - u_B)^2 + 4.328(u_L - u_B)RS \\
 & - 0.84R^2S^2] = 0.
 \end{aligned} \quad (22)$$

Equations (21) and (22) can be solved simultaneously by using the experimental values of R , u_B , and v_B to obtain the values of α and β . The resolution is performed with the software Matlab. In Fig. 12, the calculated values of α and β are compared to the values measured from image processing

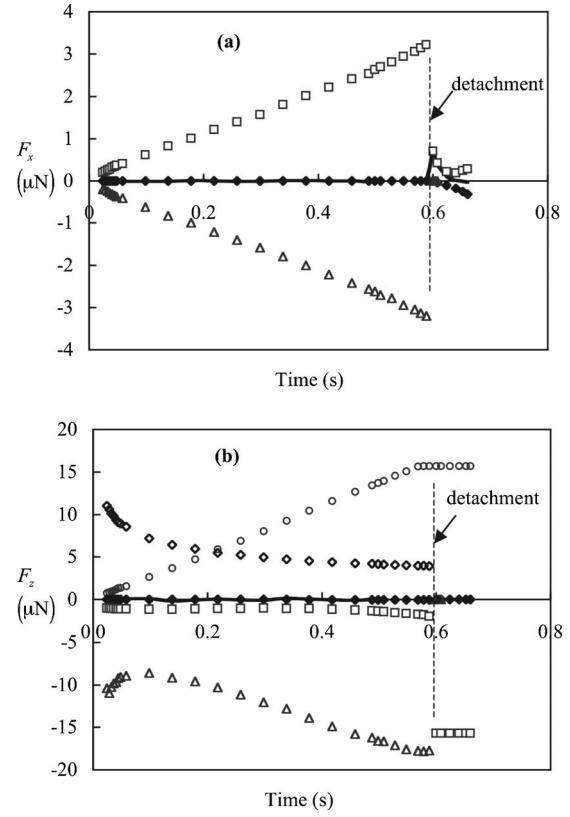


FIG. 13. Forces acting on the bubble for $Q=2.76 \text{ mm}^3/\text{s}$ and $S=5.6 \text{ s}^{-1}$ in the X direction (a) and Z direction (b): \circ , F_B , \square , F_D , \triangle , F_C , \diamond , F_{CP} , \blacklozenge , F_M , —, force balance.

for $Q=2.6 \text{ mm}^3/\text{s}$, and for two shear rates $S=5.6$ and $S=9.9 \text{ s}^{-1}$. The agreement is good and therefore Eqs. (21) and (22) seem able to reproduce the dynamics of the bubble growth in a viscous shear flow. The bubble detachment occurs when α reaches 90° . The higher the shear rate, the higher the inclination of the bubble and the smaller the value of β . For $S=5.6 \text{ s}^{-1}$, β is close to 40° just before the detachment and for $S=9.9 \text{ s}^{-1}$, $\beta \approx 20^\circ$.

In Fig. 13, the forces acting on the bubble in the X and Z directions are plotted for $Q=2.76 \text{ mm}^3/\text{s}$ and $S=5.6 \text{ s}^{-1}$. The migration force is very small throughout the bubble growth and will be neglected in the following. In the X direction, the drag force tends to detach the bubble whereas the capillary force maintains the bubble attached on the wall. The X component of the capillary force is due to the dissymmetry of the contact angles α and β . It is maximum just before the bubble detachment. It vanishes at the instant of detachment. In the Z direction, the force balance is similar to that in a quiescent liquid; the buoyancy, and the contact pressure forces act for bubble detachment and are opposed to the capillary and the drag forces.

VII. PREDICTIVE MODEL OF BUBBLE RADIUS AT DETACHMENT

The kinematic data obtained by image processing allows us to evaluate the different forces acting on a bubble

TABLE II. Geometrical and kinematic characteristics at bubble detachment.

Q (mm ³ /s)	S (s ⁻¹)	z (mm)	u_B (mm/s)	v_B (mm/s)	α (°)	β (°)	$v_B/(dR/dt)$
2.34	0	1.08	0	1.6	69		4.975
5.53	0	1.21	0	3.7	67		4.529
2.76	5.6	1.03	0.46	1.7	90	48	3.952
5.55	5.2	1.13	1.2	3.3	88	50	4.338
2.60	9.9	0.99	0.71	1.6	90	29	3.969
5.16	10.8	1.04	2.2	3.6	90	17	4.371

throughout the growth until its detachment. In the vertical direction Z , the buoyancy and the contact pressure forces tend to detach the bubble whereas the capillary and the drag forces are opposed to the detachment. The drag force is not negligible in a viscous fluid. The unsteady forces not taken into account in the model are negligible during the growth, but significant just after the detachment.

The force balance equations will be used to predict the bubble radius at detachment versus the gas flow rate Q and the shear rate S . However, we need some experimental data to simplify these equations. Namely the values of u_B and v_B at detachment must be known.

A. Experimental data

The main experimental results are gathered in Table II:

- the ratio of the vertical coordinate z of the bubble center of gravity over the bubble radius at detachment is constant for all the runs: $z/R_{\text{det}} \approx 1.5$,
- the vertical component of the bubble velocity is found to be proportional to the interface velocity:

$$v_B = C_1 \dot{R} = C_1 \frac{Q}{4\pi R^2}, \quad \text{with } 3 < C_1 < 5, \quad (23)$$

- the horizontal component of the bubble slip velocity is proportional to the shear rate:

$$u_L = Sz \approx 1.5SR_{\text{det}} \quad \text{and} \quad u_L - u_B = C_2 RS, \quad (24)$$

with $1.1 < C_2 < 1.5$,

- the values of the contact angles at detachment estimated by Eq. (19) and by Eqs. (21) and (22) are reported in Table II,
- the drag coefficient in the vertical direction has been experimentally determined: $C_{Dz} = 38/\text{Re}_B$ ($k_z = 38/16$).

B. In a quiescent liquid

In Eq. (19) v_B is replaced by Eq. (23) and an implicit relation is obtained between R to Q :

$$-\mu_L \frac{38}{16} C_1 Q + (\rho_L - \rho_G) \frac{4}{3} \pi R^4 g - 2\pi R \sigma_L r_c \sin \alpha + 2\pi \sigma_L R^2 = 0. \quad (25)$$

The value of the bubble radius at detachment R_{det} is calculated for different values of α and C_1 and compared to the experimental data in Fig. 14. The best agreement between the model and the experiments is obtained for $\alpha = 70^\circ$ and $C_1 = 2$ for gas flow rates up to 40 mm³/s. The value of α taken in the model is equal to the experimental value, whereas the value of C_1 is a little smaller in the model.

Equation (25) can also be written as

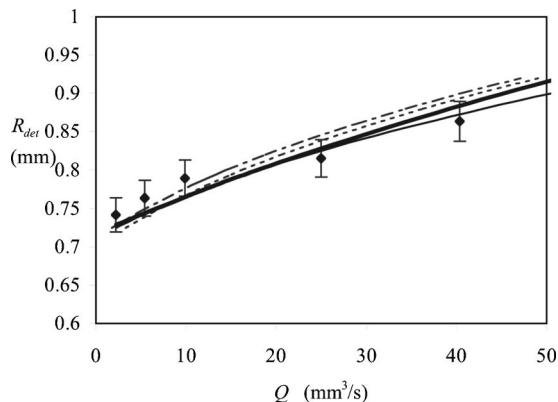


FIG. 14. Bubble radius at detachment in a quiescent liquid: \blacklozenge , $-$, R_{det} measured for $S=0$ s⁻¹; R_{det} calculated from Eq. (25) for: $-$, $\alpha=70^\circ$, $C_1=2$; $- -$, $\alpha=70^\circ$, $C_1=2.5$; $- \cdot -$, $\alpha=65^\circ$, $C_1=2.5$; R_{det} calculated from Eq. (27) for $\alpha=70^\circ$, $C_1=2$ $-$.

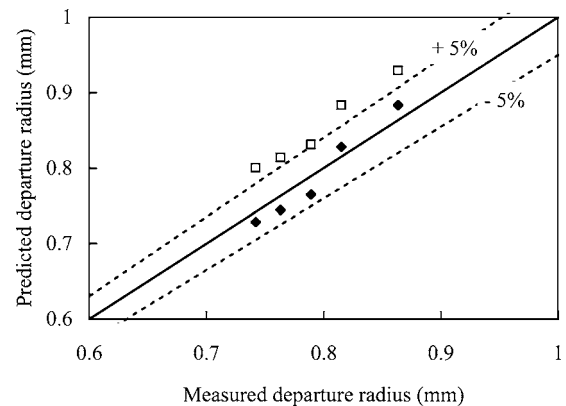


FIG. 15. Predicted departure bubble radius in a quiescent liquid: \blacklozenge , Eq. (27), \square Eq. (28).

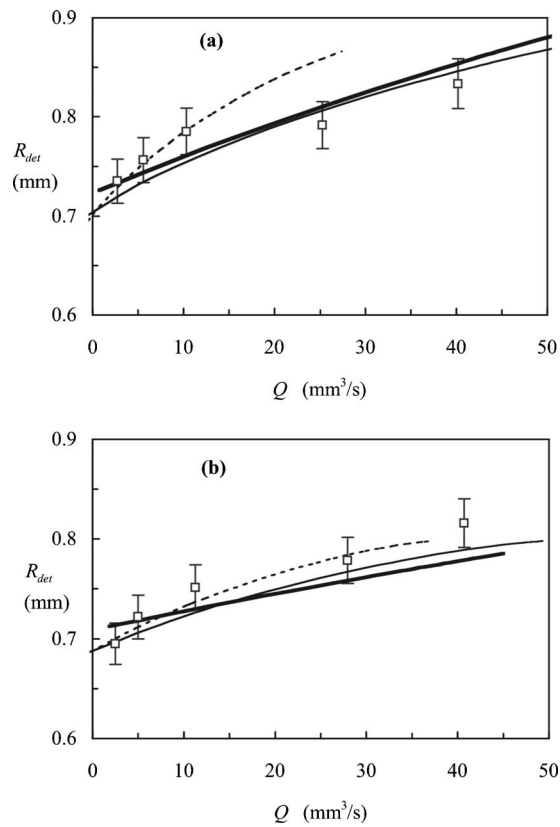


FIG. 16. Bubble radius at detachment in a shear flow: (a) $S=5.5 \text{ s}^{-1}$: \square , R_{det} measured, R_{det} calculated from Eqs. (29) and (30); —, $C_1=2$, $C_2=1.4$; - - -, $C_1=4$, $C_2=1.5$; R_{det} calculated from Eq. (34), $C_1=2$ and $C_2=1.4$ —; (b) $S=10.5 \text{ s}^{-1}$ R_{det} calculated from Eqs. (29) and (30) for $S=10.5 \text{ s}^{-1}$: —, $C_1=1.5$, $C_2=1$; - - -, $C_1=2$, $C_2=1$; R_{det} calculated from Eq. (34), $C_1=2$ and $C_2=1$ —

$$R^3 = R_F^3 \left[1 + \frac{1}{R} \left(\frac{19C_1\mu_L Q}{16\pi\sigma_L r_c \sin \alpha} - \frac{r_c}{\sin \alpha} \right) \right], \quad (26)$$

with $R_F = \sqrt[3]{\frac{3\sigma_L r_c \sin \alpha}{2(\rho_L - \rho_G)g}}$,

R_F is the bubble radius at detachment determined by Fritz (1935; see Kumar and Kuloor²¹) from a balance between buoyancy and capillary forces. By replacing $1/R$ by $1/R_F$, an explicit approximate expression for the bubble departure diameter is obtained:

$$R = R_F \left[1 + \frac{1}{R_F} \left(\frac{19\mu_L Q}{8\pi\sigma_L r_c \sin \alpha} - \frac{r_c}{\sin \alpha} \right) \right]^{1/3}, \quad \text{with } C_1 = 2. \quad (27)$$

This expression is also plotted in Fig. 14 for $C_1=2$ and $\alpha=70^\circ$. It differs from the values obtained by Eq. (25) only for the higher values of Q , for which the drag force is not small before the capillary force. However, the deviation between the two equations is smaller than 4% for $Q=50 \text{ mm}^3/\text{s}$.

Several models for the prediction of bubble departure diameters exist. But most of them only take into account two dominant forces^{2,3,11}: gravity/capillary forces or gravity/added mass forces or gravity/viscous forces. Gaddis and

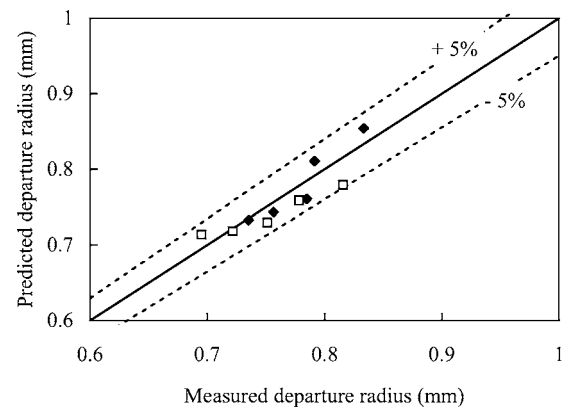


FIG. 17. Predicted departure radii in a shear flow using Eq. (34): \blacklozenge , for $S=5.5 \text{ s}^{-1}$, \square for $S=10.5 \text{ s}^{-1}$.

Vogelpohl⁶ established a model including the gravity, the drag, and the added mass forces. They provided the following approximate solution valid for a wide range of liquid viscosities and gas flow rates:

$$2R = \left[\left(\frac{12r_c\sigma_L}{\rho_L g} \right)^{4/3} + \left(\frac{81\mu_L Q}{\rho_L \pi g} \right) + \left(\frac{153Q^2}{4\pi^2 g} \right)^{4/5} \right]^{1/4}. \quad (28)$$

The main differences with our model are the value of the drag coefficient ($=1+24/\text{Re}_B$), the value of $\alpha=90^\circ$ in the capillary force, the presence of the added mass force (the third term in the brackets) and the absence of the contact pressure force. A comparison of the departure diameters predicted by Eqs. (27) and (28) is plotted in Fig. 15. The values given by the model of Gaddis and Vogelpohl are larger because the contact pressure force is not taken into account and the drag force is higher. The added mass force has no effect.

C. In a shear flow

In the case of a growing bubble in a shear flow the force balance equations written in the X and Z directions become after neglecting the migration forces in Eqs. (21) and (22):

$$\begin{aligned} & -1.25 \times 2\sigma_L r_c \frac{\pi(\alpha - \beta)}{\pi^2 - (\alpha - \beta)^2} (\sin \alpha + \sin \beta) \\ & + \frac{11}{8} \mu_L \pi R \left(4(u_L - u_B) - \frac{1}{2} RS \right) = 0, \\ & (\rho_L - \rho_G) \frac{4}{3} \pi R^3 g - 2\sigma_L r_c \frac{\pi}{\alpha - \beta} (-\cos \alpha + \cos \beta) \\ & + \frac{2\pi\sigma_L}{R} r_c^2 - 4\pi\mu_L R v_B k_z = 0. \end{aligned}$$

By using Eqs. (23) and (24), these equations become

$$\begin{aligned} & -1.25 \times 2\sigma_L r_c \frac{\pi(\alpha - \beta)}{\pi^2 - (\alpha - \beta)^2} (\sin \alpha + \sin \beta) \\ & + \frac{11}{8} \mu_L \pi R^2 S \left(4C_2 - \frac{1}{2} \right) = 0, \end{aligned} \quad (29)$$

$$(\rho_L - \rho_G) \frac{4}{3} \pi R^3 g - 2 \sigma_L r_c \frac{\pi}{\alpha - \beta} (-\cos \alpha + \cos \beta) + \frac{2 \pi \sigma_L}{R} r_c^2 - \frac{38}{16} \mu_L \frac{C_1 Q}{R} = 0. \quad (30)$$

For a given couple of parameters (Q , S) and for a value of α equal to 90° at detachment, Eqs. (29) and (30) can be solved numerically to obtain the two unknowns of the problem: the angle β and the bubble radius at detachment R_{det} . In Fig. 16, the values of R_{det} calculated by these equations are plotted for two shear rates $S=5.5$ and $S=10.5 \text{ s}^{-1}$ and different values of the constants C_1 and C_2 . For a shear rate of 5.5 s^{-1} , the best agreement between the model and the experiments is obtained for $C_1=4$ and $C_2=1.5$ for $Q < 15 \text{ mm}^3/\text{s}$. These values are in conformity with those of Eqs. (23) and (24). For gas flow rates greater than $20 \text{ mm}^3/\text{s}$ the values of $C_1=2$ and $C_2=1.4$ provide a better prediction. The value of β calculated by the model is equal to 48° for $Q=2 \text{ mm}^3/\text{s}$ and decreases to 25° for $Q=40 \text{ mm}^3/\text{s}$.

For a higher shear rate $S=10.5 \text{ s}^{-1}$, the values of $C_2=1$ and $C_1=2$ or 1.5 have been used in the model. β decreases from 38° to 10° for gas flow rates between 2 and $40 \text{ mm}^3/\text{s}$.

The model is able to predict the bubble departure diameter with good accuracy. Nevertheless, it requires an implicit resolution of two coupled equations, which is not very convenient. Therefore a reduction of this model to an explicit expression of R_{det} is now proposed. Equations (29) and (30) can be written in a dimensionless form:

$$f(\beta) = \frac{\pi/2 - \beta}{\pi^2 - (\pi/2 - \beta)^2} (1 + \sin \beta) = \frac{11 R_0}{20 r_c} \text{Ca} \left(\frac{R}{R_0} \right)^2,$$

$$\text{with } R_0 = \sqrt[3]{\frac{3 \sigma_L r_c}{2(\rho_L - \rho_g)g}}$$

$$\text{and } \text{Ca} = \frac{\mu_L R_0 S (4C_2 - 1/2)}{\sigma_L}, \quad (31)$$

$$\left(\frac{R}{R_0} \right)^3 = g(\beta) + \left(\frac{19}{16} \frac{\mu_L C_1 Q}{\pi \sigma_L r_c R_0} - \frac{r_c}{R_0} \right) \frac{R_0}{R}; \quad (32)$$

$$g(\beta) = \frac{\cos \beta}{\pi/2 - \beta},$$

where R_0 is a characteristic radius and Ca a capillary number. Here $f(\beta)$ and $g(\beta)$ are monotonously decreasing functions of β . For each value of $\text{Ca}(R/R_0)^2$, the values of $f(\beta)$, β , and $g(\beta)$ are calculated. Here $g(\beta)$ is a decreasing function of $\text{Ca}(R/R_0)^2$, which is fitted by the following polynomial law:

$$g(\beta) = 0.13 + 11.44 \left(\frac{11 R_0}{20 r_c} \right) \text{Ca} \left(\frac{R}{R_0} \right)^2 - 42 \left(\frac{11 R_0}{20 r_c} \right)^2 \text{Ca}^2 \left(\frac{R}{R_0} \right)^4. \quad (33)$$

If we assume that R_0 is a first order approximation of R , R can be expressed versus a small parameter ε : $R = R_0(1 + \varepsilon)$. An expansion of Eq. (32) at order ε , using Eq. (33) yields to

$$R = R_0 \left(1 + \frac{0.13 + 11.44 \left(\frac{11 R_0}{20 r_c} \right) \text{Ca} - 42 \left(\frac{11 R_0}{20 r_c} \right)^2 \text{Ca}^2 + \left(\frac{19}{16} \frac{\mu_L C_1 Q}{\pi \sigma_L r_c R_0} - \frac{r_c}{R_0} \right) - 1}{3 - 22.88 \left(\frac{11 R_0}{20 r_c} \right) \text{Ca} + 168 \left(\frac{11 R_0}{20 r_c} \right)^2 \text{Ca}^2 + \left(\frac{19}{16} \frac{\mu_L C_1 Q}{\pi \sigma_L r_c R_0} - \frac{r_c}{R_0} \right)} \right). \quad (34)$$

The values of R_{det} predicted by Eq. (34) are plotted in Fig. 16. This approximate expression is simpler to use than Eqs. (29) and (30) to predict the bubble departure diameter and the accuracy remains good, less than 5%, as can be seen in Fig. 17.

It is not very easy to compare the results of our model with those of the other existing models. Al-Hayes and Winterton⁹ determine a departure criterion for bubbles on inclined surfaces based on a balance of the drag, the buoyancy, and the capillary forces in the direction parallel to the wall. This balance roughly corresponds to Eq. (29) of our model for horizontal surfaces and the predicted departure diameters are around 1 mm but are independent of Q . More complete models allow calculating the evolutions of the bubble radius and of the bubble center of gravity using force

balance models. Marshall *et al.*¹⁰ derive a theoretical model for gas bubble formation in a liquid cross flow using the potential flow theory. A “bubble pressure minimum” criterion is used to predict the bubble detachment. Another model is proposed by Nahra and Kamonati⁷ for the prediction of the bubble diameter at detachment in normal and microgravity conditions in liquid cross flows. They consider a force balance, taking into account all the forces (buoyancy, added mass, lift, drag, capillary, contact pressure forces). They solve a system of two coupled differential equations to calculate the time evolution of x and z coordinates of the bubble center of gravity. In this paper the criterion for bubble detachment is based on a critical value of the distance between the bubble center and the injection orifice position. These two models^{10,7} require the numerical resolution of coupled

differential equations and no analytical expression for the bubble departure diameter is provided. It is therefore not possible to compare directly the results of these models with our results, as was the case for a quiescent liquid.

VIII. CONCLUSION

Bubble growth and detachment in a viscous shear flow has been experimentally studied from high-speed visualizations and image processing. Time-evolutions of bubble radius and position of the center of gravity have been used to estimate the different forces acting on the bubble. The theoretical results of Magnaudet *et al.*¹⁶ on bubble motion near a wall in a weakly inertial regime have been extrapolated to a bubble growing at the wall in a shear flow. The force balance during the bubble growth shows that the contact angles α and β continuously evolve throughout the growth. Finally, a force balance model is proposed to predict the detachment of one bubble in the quasistatic regime and for a small bubble Reynolds numbers. The detachment occurs when the capillary force reaches its maximal value, given by the value of the advancing contact angle α : $\alpha \approx 70^\circ$ in a quiescent liquid and $\alpha \approx 90^\circ$ in a shear flow. The bubble radius at detachment can then be calculated in a quiescent liquid by using Eq. (27) and in shear flow by using Eqs. (29) and (30) for gas flow rates Q up to $40 \text{ mm}^3/\text{s}$ and shear rates S up to 11 s^{-1} . Since the resolution of the force balance model is implicit, a reduction of this model has been performed in order to provide explicit expressions for the bubble radius at detachment in a quiescent liquid [Eq. (27)] and in a shear flow [Eq. (34)]. These expressions are very simple to use and give the bubble departure radius with good accuracy (less than 5%). They are able to reproduce the increase in R_{det} by increasing the gas flow rate Q and decreasing the shear rate S or the capillary number.

¹S. S. Sadhal, P. S. Ayyaswamy, and J. N. Chuang, *Transport Phenomena With Drop and Bubbles* (Springer-Verlag, New York, 1997).

²J. F. Davidson and B. O. G. Schüller, "Bubble formation at an orifice in a viscous liquid," *Trans. Inst. Chem. Eng.* **38**, 144 (1960).

- ³A. Marmur and E. Rubin, "A theoretical model for bubble formation at a submerged orifice in an inviscid liquid," *Chem. Eng. Sci.* **11**, 453 (1976).
- ⁴D. J. McCann and G. H. Prince, "Regimes of bubbling at a submerged orifice," *Chem. Eng. Sci.* **26**, 1505 (1971).
- ⁵N. Rübiger and A. Vogelpohl, "Bubble formation and its movement in Newtonian and non Newtonian liquids," *Encyclopedia of Fluid Mechanics*, edited by X. Cheremisinoff (Gulf, Houston, TX, 1986), Chap. 4, p. 43.
- ⁶E. S. Gaddis and A. Vogelpohl, "Bubble formation in quiescent liquid under flow conditions," *Chem. Eng. Sci.* **41**, 97 (1986).
- ⁷H. K. Nahra and Y. Kamonati, "Bubble formation from wall orifice in liquid cross flow under low gravity," *Chem. Eng. Sci.* **55**, 4653 (2000).
- ⁸G. E. Thorncroft, J. F. Klausner, and R. Mei, "Bubble forces and detachment models," *Multiphase Sci. Technol.* **13**, 35 (2001).
- ⁹R. A. M. Al-Hayes and R. H. S. Winterton, "Bubble diameter on detachment in flowing liquid," *Int. J. Heat Mass Transfer* **24**, 223 (1981).
- ¹⁰S. H. Marshall, M. W. Chudacek, and D. F. Bagster, "A model for bubble formation from an orifice with liquid cross-flow," *Chem. Eng. Sci.* **48**, 2048 (1993).
- ¹¹H. N. Oguz and A. Prosperetti, "Dynamics of bubble growth and detachment from a needle," *J. Fluid Mech.* **257**, 111 (1993).
- ¹²K. Terasaka and H. Tsuge, "Bubble formation at a single orifice in highly viscous liquid," *J. Chem. Eng. Jpn.* **23**, 160 (1990).
- ¹³H. Z. Li, Y. Mouline, and N. Midoux, "Modelling the bubble formation dynamics in non-Newtonian fluids," *Chem. Eng. Sci.* **57**, 339 (2002).
- ¹⁴H. Tsuge, Y. Tannaka, K. Terasaka, and M. Hirokazu, "Bubble formation in flowing liquid under reduced gravity," *Chem. Eng. Sci.* **52**, 3671 (1997).
- ¹⁵W. Zhang and R. B. H. Tan, "A model for bubble formation and weeping at submerged orifice with liquid cross-flow," *Chem. Eng. Sci.* **58**, 287 (2003).
- ¹⁶J. Magnaudet, S. Takagi, and D. Legendre, "Drag, deformation and lateral migration of a buoyant drop moving near a wall," *J. Fluid Mech.* **476**, 115 (2003).
- ¹⁷T. H. Cohran and J. Aydelott, "The effect of subcooling and gravity level on boiling in the discrete bubble regime," NASA Technical Note TN D-3449, 1966.
- ¹⁸J. F. Klausner, R. Mei, M. D. Bernhard, and L. Z. Zeng, "Vapour bubble departure in forced convection boiling," *Int. J. Heat Mass Transfer* **36**, 651 (1993).
- ¹⁹J. Magnaudet, "Small inertial effects on a spherical bubble, drop or particle moving near a wall in a time-dependent linear flow," *J. Fluid Mech.* **485**, 115 (2003).
- ²⁰G. Duhar, "Croissance et détachement de bulles en paroi d'un écoulement cisaillé: étude expérimentale de l'injection et de l'ébullition nucléée," Ph.D. thesis, Institut National Polytechnique de Toulouse, France, 2003.
- ²¹R. Kumar and N. R. Kuloor, "The formation of bubbles and drops," *Adv. Chem. Eng.* **8**, 256 (1970).